Eur. Phys. J. Special Topics **224**, 401–413 (2015)

DOI: 10.1140/epjst/e2015-02369-y

THE EUROPEAN PHYSICAL JOURNAL SPECIAL TOPICS

Regular Article

# Numerical simulation of particle-laden droplet evaporation with the Marangoni effect

G. Son[a]

Department of Mechanical Engineering, Sogang University, Seoul 121-742, South Korea

Received 29 July 2014 / Received in final form 16 February 2015
Published online 8 April 2015

**Abstract.** A comprehensive numerical method for analysis of the evaporation of a particle-laden microdroplet is developed including the effects of heat and mass transfer, phase change, dynamic contact angles, Marangoni force, and particle concentration. A level-set method, which can easily handle the liquid-gas interface with change in topology, is employed to solve the conservation equations of mass, momentum and energy in the liquid and gas phases, vapor concentration in the gas phase, and particle concentration in the liquid phase with sharp-interface numerical techniques for the boundary conditions at the interface. The numerical method is applied to microdroplet evaporation on a solid surface to investigate the Marangoni effect on the droplet evaporation and particle distribution.

## 1 Introduction

The evaporation of a particle-laden microdroplet has received significant attention as an efficient and low-cost fabrication process for microstructures. Efforts have been made to develop a predictive model for the evaporation process involving multiphase dynamics of liquid, gas, vapor, and solid particles.

Deegan et al. [1] theoretically predicted the particle distribution in droplet evaporation on a solid surface simplifying the droplet shape and the conservation equations of momentum and particle concentration and using an approximate expression for the evaporation rate. Their analysis proved that the particle accumulation or coffee-ring formation near the pinned liquid-gas-solid contact line resulted from the increased evaporation rate in that region. Fischer [2] showed that the particle deposition pattern could be changed by varying the evaporation condition and thus the internal flow of the droplet.

For its more general prediction, numerical simulations of particle-laden droplet evaporation were performed in several studies. Widjaja and Harris [3] simulated the evaporation process using a finite element method (FEM) to solve a diffusion equation for the vapor fraction and an advection-diffusion equation for the particle concentration. Bhardwaj et al. [4] extended the FEM analysis for the particle deposition by including the effects of heat transfer and wettability. Maki and Kumar [5] computed the particle transport in the evaporation of a spreading droplet employing body-fitted

[a] e-mail: gihun@sogang.ac.kr

moving grids for the interface region combined with Cartesian grids for the remaining region. They demonstrated the formation of a layer of particles on the droplet surface and the particle accumulation at the droplet edge to produce a coffee ring. However, the Lagrangian methods are generally not straightforward to implement for breaking or merging of the interface. Recently, Fujita et al. [6] performed direct numerical simulation of individual particles in drying colloidal suspension by combining an immersed boundary method for particle-fluid interaction and a level-set (LS) interface tracking method based on diffuse-interface modeling. Their formulation was simplified by assuming the vaporization mass flow rate was constant rather than solving the conservation equations of energy and vapor fraction.

In this study, a LS method, which can easily handle the liquid-gas interface with change in topology, is developed for comprehensive simulation of particle-laden droplet evaporation including the effects of Marangoni force and particle concentration as well as the effects of heat and mass transfer, evaporation, and dynamic contact angles.

## 2 Numerical analysis

The present numerical approach is based on the sharp-interface LS formulation developed by Son [7–9] for droplet evaporation and Lee and Son [10] for particle motion. The LS method is extended for analysis of particle-laden droplet evaporation with the Marangoni effect caused by the gradient of surface tension coefficient. The droplet surface is tracked by the LS function $\phi$, which is defined as a signed distance from the liquid-gas interface. The negative sign is chosen for the gas phase and the positive sign for the liquid phase. In this work, the following assumptions are made:

(1) the gas phase is an ideal mixture of air and vapor;
(2) the liquid phase is a mixture of evaporating liquid and non-evaporating particles;
(3) the wall temperature is below the boiling temperature;
(4) the interface has no thickness;
(5) the temperature is continuous at the interface.

The fourth and fifth assumptions are not valid when the droplet size is of the order of a few tens of nanometers, which is comparable to the interface thickness or the mean free path of a gas, as addressed in Refs. [11–13]. However, they are not so restrictive in the present work considering the initial droplet size of the order of a few tens of micrometers. In this work, we do not consider the contact angle between each individual particle and the liquid-gas interface. The contact angle effect can be estimated only when direct numerical simulation of individual particles is conducted, which will be done in the future.

Based on the ghost fluid method (GFM) [14–16], which is a sharp-interface numerical technique for accurately enforcing the boundary conditions at the interface, the conservation equations of mass, momentum and energy in the liquid and gas phases, vapor mass fraction ($Y_v$) in the gas phase, and particle volume fraction ($Y_p$) in the liquid phase can be expressed as

$$\nabla \cdot \mathbf{u} = \beta \dot{m} \mathbf{n} \cdot \nabla \alpha \tag{1}$$

$$\hat{\rho}\left(\frac{\partial \mathbf{u}}{\partial t} + \mathbf{u}_f \cdot \nabla \mathbf{u}_f\right) = -[\nabla p + (\sigma\kappa - \beta\dot{m}^2)\nabla\alpha] + \mathbf{f}_M + \nabla \cdot \hat{\mu}[\nabla \mathbf{u} - (\beta \dot{m} \mathbf{n} \nabla \alpha)^T + (\nabla \mathbf{u}_f)^T] \tag{2}$$

$$\rho_f c_f \left( \frac{\partial T_f}{\partial t} + \mathbf{u}_f \cdot \nabla T_f \right) = \nabla \cdot \hat{\lambda}_f \nabla T_f \quad \text{if } \phi \neq 0 \tag{3}$$

$$T_f = T_I \quad \text{if } \phi = 0 \tag{4}$$

$$\frac{\partial Y_v}{\partial t} + \mathbf{u}_g \cdot \nabla Y_v = \nabla \cdot \hat{D}_v \nabla Y_v \quad \text{if } \phi < 0 \tag{5}$$

$$Y_v = Y_{v,I} \quad \text{if } \phi = 0 \tag{6}$$

$$\frac{\partial Y_p}{\partial t} + \mathbf{u}_l \cdot \nabla Y_p = \nabla \cdot \hat{D}_p \nabla Y_p \quad \text{if } \phi > 0 \tag{7}$$

$$(\mathbf{u}_l - \mathbf{U}) \cdot \mathbf{n} Y_p = \hat{D}_p \nabla Y_p \cdot \mathbf{n} \quad \text{if } \phi = 0 \tag{8}$$

where

$$\alpha = 1 \quad \text{if } \phi > 0 \tag{9}$$

$$\alpha = 0 \quad \text{if } \phi \leq 0 \tag{10}$$

$$\beta = \rho_g^{-1} - \rho_l^{-1} \tag{11}$$

$$\mathbf{n} = \nabla\phi / |\nabla\phi| \tag{12}$$

$$\kappa = \nabla \cdot \mathbf{n} \tag{13}$$

$$\hat{\rho} = \rho_g (1 - F_l) + \rho_l F_l \tag{14}$$

$$\hat{\mu}^{-1} = \mu_g^{-1} (1 - F_l) + \mu_l^{-1} F_l \tag{15}$$

$$\hat{\lambda}_g^{-1} = \lambda_g^{-1} (1 - F_l) \tag{16}$$

$$\hat{\lambda}_l^{-1} = \lambda_l^{-1} F_l \tag{17}$$

$$\hat{D}_v^{-1} = D_v^{-1} (1 - F_l) \tag{18}$$

$$\hat{D}_p^{-1} = D_p^{-1} F_l. \tag{19}$$

Here, $\mathbf{u}$ is the velocity, $p$ the pressure, and $T$ the temperature. The subscript $f$ denotes the liquid phase ($l$) for $\phi > 0$ and the gas phase ($g$) for $\phi \leq 0$. The discontinuous step function $\alpha$, the interface normal $\mathbf{n}$, and the interface curvature $\kappa$ are evaluated from the LS function. The surface tension coefficient $\sigma$ is assumed to be a linear function of interface temperature

$$\sigma = \sigma_{\text{ref}} - |\sigma_T| (T - T_{\text{ref}}). \tag{20}$$

The velocity $\mathbf{u}_f$ ($\mathbf{u}_l$ or $\mathbf{u}_g$) for each phase is extrapolated into the entire domain (or a narrow band near the interface) from the real velocity. For example, the ghost liquid velocity at $\phi \leq 0$ is evaluated by the first-order extrapolation from the real liquid velocity at $\phi > 0$. The effective density $\hat{\rho}$, viscosity $\hat{\mu}$, thermal conductivity $\hat{\lambda}$, vapor diffusion coefficient $\hat{D}_v$, and particle diffusion coefficient $\hat{D}_p$ are interpolated by using a fraction function $F_l$, which is defined as

$$\begin{aligned} F_l &= 1 && \text{if } \alpha(\phi_A) = \alpha(\phi_B) = 1 \\ &= 0 && \text{if } \alpha(\phi_A) = \alpha(\phi_B) = 0 \\ &= \frac{\max(\phi_A, \phi_B)}{\max(\phi_A, \phi_B) - \min(\phi_A, \phi_B)} && \text{otherwise} \end{aligned}$$

where the subscripts $A$ and $B$ denote the grid points adjacent to the location where $F_l$ is evaluated. The temperature $T_I$ and the vapor fraction $Y_{v,I}$ at the interface ($\phi = 0$) and the evaporation mass flux $\dot{m}$ are simultaneously determined from the following coupled equations for the mass and energy balances at the interface and the thermodynamic relation

$$\dot{m} = \frac{\mathbf{n} \cdot \rho_g D_v (\nabla Y_v)_g}{(1 - Y_{v,I})} = \frac{\mathbf{n} \cdot [\lambda_l (\nabla T)_l - \lambda_g (\nabla T)_g]}{h_{lg}} \tag{21}$$

$$Y_{v,I} = \frac{M_v p_{v,sat}(T_I)}{M_v p_{v,sat}(T_I) + M_a [p_\infty - p_{v,sat}(T_I)]} \tag{22}$$

where $h_{lg}$ is the latent heat of vaporization, $p_\infty$ the ambient pressure, $p_{v,sat}$ the saturated vapor pressure, $M_a$ the air molecular mass, and $M_v$ the vapor molecular mass. This simultaneous calculation procedure is preferred to the sequential calculation for high evaporation rate cases. Its implementation is described in Ref. [7]. For 1-D case of $\phi_i < 0 < \phi_{i+1}$, Eq. (21) can be expressed as

$$\frac{\rho_g D_g}{1 - Y_{v,I}} \frac{Y_{v,i} - Y_{v,I}}{\phi_i} = \frac{\lambda_{i+1}}{h_{lg}} \frac{T_{i+1} - T_I}{\phi_{i+1}} - \frac{\lambda_i}{h_{lg}} \frac{T_i - T_I}{\phi_i}.$$

When $Y_{v,i}$, $T_i$ and $T_{i+1}$ are treated explicitly and $Y_{v,I}$ is a function of $T_I$ as given by Eq. (22), the above equation is solved for the interface temperature $T_I$ using a Newton-Raphson iterative algorithm. $Y_{v,I}$ and $\dot{m}$ are then obtained from Eqs. (22) and (21). This kind of interfacial boundary conditions are possibly not needed when using a diffuse-interface method supplemented by the van der Waals equation of state [11]. However, the diffuse-interface modeling will require a special technique to maintain the interface thickness without being smeared if it is applied to two-phase flows with large liquid-gas density ratios, as in the present study. The sharp-interface LS method has the advantages in reducing the numerical diffusion. The interface velocity $\mathbf{U}$ is evaluated using the real or ghost liquid velocity as

$$\mathbf{U} = \mathbf{u}_l + \frac{\dot{m}}{\rho_l}. \tag{23}$$

To consider the case where the particle concentration reaches the maximum value (in random packing) of $Y_p = 0.64$, the liquid viscosity is evaluated as [17,18]

$$\mu_l = \mu_{lo} \left(1 - \frac{Y_p}{0.64}\right)^{-1.6}. \tag{24}$$

The diffusion coefficient $D_p$ of particles is determined from the generalized Stokes-Einstein equation [19,20]

$$D_p = D_{po}(1 - Y_p)^6 \frac{1 + 4.875 Y_p + 7.441 Y_p^2 - 2.219 Y_p^3 - 65.61 Y_p^4 + 68.097 Y_p^5}{(1 - Y_p/0.64)^2}. \tag{25}$$

The dilute limit $D_{po}$ is expressed as $D_{po} = k_B T / 3\pi \mu_l d_p$, where $k_B$ is the Boltzmann constant and $d_p$ is the particle diameter.

Introducing the delta function $|\nabla \alpha|$, as done in Refs. [21,22], the Marangoni force $\mathbf{f}_M$ can be formulated as

$$\mathbf{f}_M = (\nabla_s \sigma) |\nabla \alpha| \tag{26}$$

where $\nabla_s \sigma = \nabla \sigma - \mathbf{n}(\mathbf{n} \cdot \nabla \sigma)$. However, this delta function formulation is not appropriate for prediction of the flow field in the gas region, as observed in Ref. [9] while

computing two-phase Marangoni convection in a cavity. We use a sharp-interface formulation of $\mathbf{f}_M$ developed in Ref. [9] for good convergence in both the liquid and gas regions. The formulation can be derived by following the discretization procedure of Kang et al. [14] for the viscous terms. In a staggered grid system where the velocity components are defined at cell faces whereas the other dependent variables at cell centers, it can be written as

$$(\mathbf{f}_M)_{p,q} = \left(\hat{\mu}\nabla_s\sigma|\frac{\partial\alpha}{\partial r}|\right)_{p-1/2,q} + \left(\hat{\mu}\nabla_s\sigma|\frac{\partial\alpha}{\partial r}|\right)_{p+1/2,q}$$

$$+ \left(\hat{\mu}\nabla_s\sigma|\frac{\partial\alpha}{\partial y}|\right)_{p,q-1/2} + \left(\hat{\mu}\nabla_s\sigma|\frac{\partial\alpha}{\partial y}|\right)_{p,q+1/2} \tag{27}$$

where the axisymmetric coordinates (r, y) are used and the subscript (p, q) refers to the grid point where the velocity component is defined. The viscosity function $\hat{\mu}$ is expressed as

$$\hat{\mu}_{p\pm1/2,q} = \frac{\mu^{-1}_{p\pm1,q}|\phi_{p\pm1,q}|}{\mu^{-1}_{p,q}|\phi_{p,q}| + \mu^{-1}_{p\pm1,q}|\phi_{p\pm1,q}|} \tag{28}$$

$$\hat{\mu}_{p,q\pm1/2} = \frac{\mu^{-1}_{p,q\pm1}|\phi_{p,q\pm1}|}{\mu^{-1}_{p,q}|\phi_{p,q}| + \mu^{-1}_{p,q\pm1}|\phi_{p,q\pm1}|}. \tag{29}$$

The LS function $\phi$ is advanced and reinitialized as

$$\frac{\partial\phi}{\partial t} + \mathbf{U}\cdot\nabla\phi = 0 \tag{30}$$

$$\frac{\partial\phi}{\partial\tau} = \frac{\phi}{\sqrt{\phi^2+h^2}}(1-|\nabla\phi|) \quad \text{if} \quad |\phi| \geq h/2 \tag{31}$$

where $h$ is a grid spacing.

While considering the particle motion in an evaporating microdroplet, the liquid flow inside the droplet is important although it is much weaker than the gas flow caused by the droplet evaporation. The low liquid velocity can be easily influenced by the numerical errors in discretizing the surface tension force, even without including the Marangoni effect. When the LS formulation was applied to 2-D computation of particle motion in an evaporating spherical droplet in our previous study [10], the result for the particle distribution was significantly deviated from the spherical symmetry. As an effort to reduce the numerical errors, we tested the calculation procedure for the interface curvature proposed by Sussman and Ohta [23] and Sussman [24], which was originally developed to relax the time constraint caused by the explicit treatment of surface tension. The interface curvature is evaluated solving the following equation for volume-preserving motion by mean curvature (or a kind of diffusion equation) with smaller time steps:

$$\frac{d^{l+1}-d^l}{\Delta t/N} = \kappa^l - \kappa^0_{av} \qquad \text{with} \quad d^0 = \phi^{n+1} \tag{32}$$

$$\frac{\partial d^{l+1}}{\partial\tau} = \frac{d^{l+1}}{\sqrt{(d^{l+1})^2+h^2}}(1-|\nabla d^{l+1}|) \quad \text{if} \quad d^{n+1} \geq h/2 \tag{33}$$

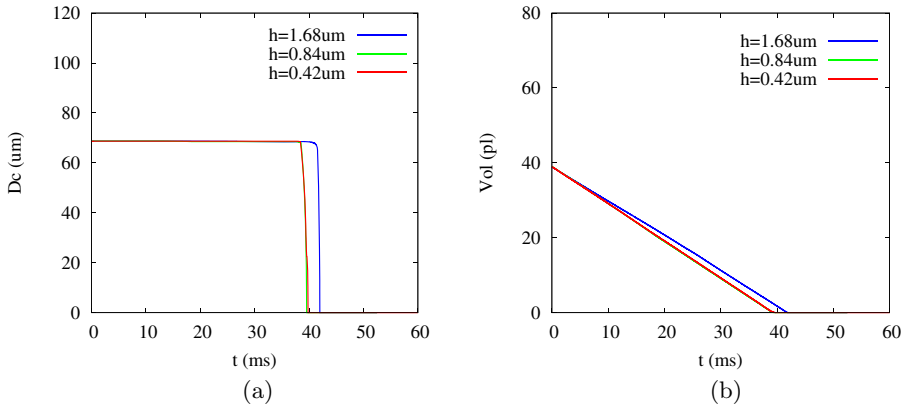


(a) (b)

**Fig. 1.** Effect of mesh size on microdroplet evaporation with the Marangoni effect: (a) droplet-wall contact diameter and (b) droplet volume.

for $l = 0, 1, ..., N-1$. Here, $\kappa = \nabla \cdot (\nabla d/|\nabla d|)$ and $\kappa_{av}$ is the average curvature. We have to choose $N$ to be proportional to $1/h$. The resultant $d^N$ is used to determine the interface curvature $\kappa$ in the momentum equation,

$$\kappa = \frac{d^N - d^0}{\Delta t}. \tag{34}$$

When using the modified formulation of the interface curvature, the results for droplet internal flow and particle distribution can be significantly improved, as seen in Ref. [10].

While discretizing the governing equations temporally, we use a first-order explicit scheme for the convection and source terms and a fully implicit scheme for the diffusion terms. The mass and momentum equations are solved by employing the projection method. A second-order essentially nonoscillatory (ENO) scheme is used for the convection terms and the distance function and a second-order central difference scheme for the other terms including the diffusion terms and the interface curvature. The interface curvature $\kappa$ is interpolated to the zero LS for the interface. For example, $\kappa_{i\pm1/2,j}$ is expressed for $\phi_{i,j}\phi_{i\pm1,j} < 0$ as

$$\kappa_{i\pm1/2,j} = \frac{\phi_{i,j}\kappa_{i\pm1,j} - \phi_{i\pm1,j}\kappa_{i,j}}{\phi_{i,j} - \phi_{i\pm1,j}}. \tag{35}$$

## 3 Results and discussion

The sharp-interface LS formulation is applied to particle-laden droplet evaporation on a solid surface. The computational domain is chosen as a cylindrical region of $0 \le r \le L$ and $0 \le y \le H$. We impose the slip condition at $r = 0$, the open boundary condition at $r = L$ or $y = H$, and the following no-slip condition at the bottom wall ($y = 0$):

$$\mathbf{u} = 0, \quad T = T_w, \quad \frac{\partial Y_v}{\partial y} = \frac{\partial Y_p}{\partial y} = 0, \quad \frac{\partial \phi}{\partial y} = -\cos\theta \tag{36}$$

where $\theta$ is a contact angle formed on the liquid-gas-solid contact line and is used to determine the LS function at the wall. The typical contact angle varies dynamically

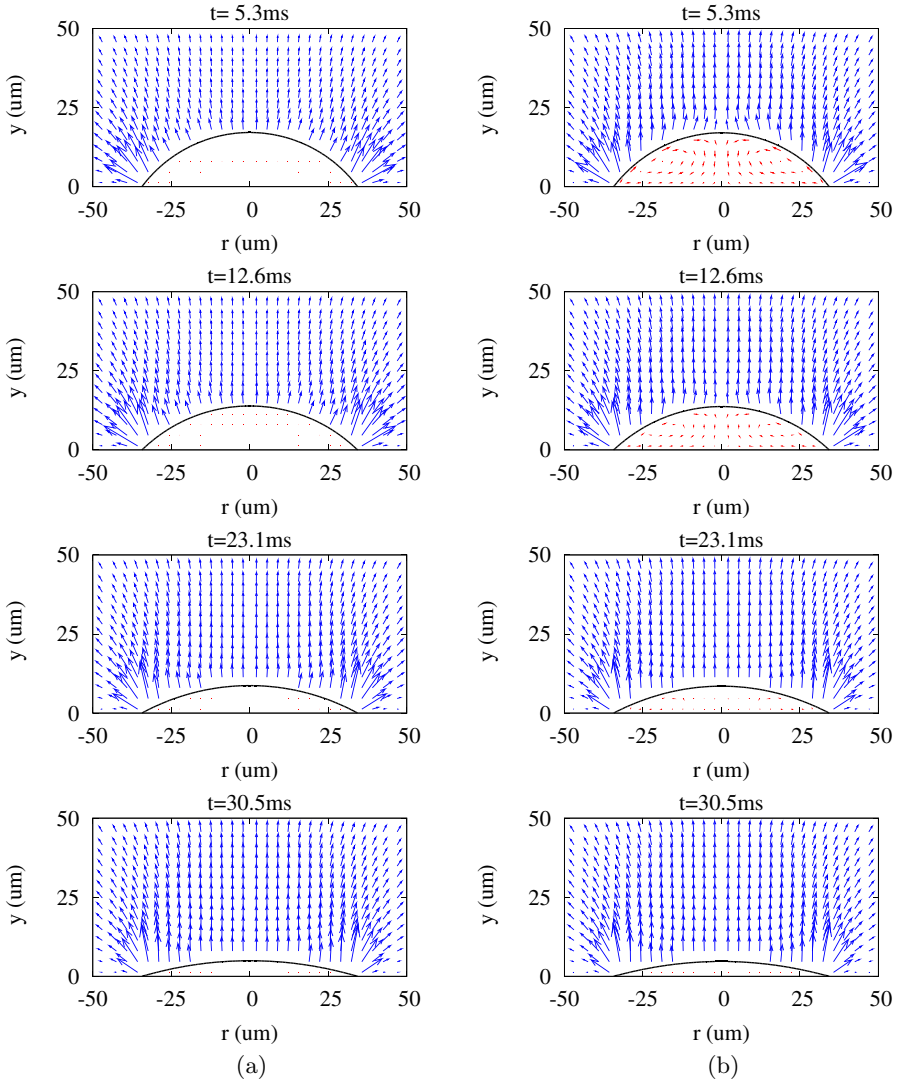


**Fig. 2.** Droplet motions and velocity fields in microdroplet evaporation (a) without and (b) with the Marangoni effect.

between an advancing contact angle $\theta_a$ and a receding contact angle $\theta_r$, as described by Fukai et al. [25]. The contact line does not move when the contact angle changes in the range $\theta_r < \theta < \theta_a$. Otherwise, while the contact line moves, the contact angle remains constant as $\theta{=}\theta_r$ or $\theta{=}\theta_a$. To simulate the contact line pinning phenomena, which occur in the evaporation of a droplet including particles, the receding contact angle is set to $\theta_r = 0$.

The calculations are carried out using the water and air properties at 1 atm: $\rho_l = 997\,\mathrm{kg/m^2}$, $\rho_g = 1.18\,\mathrm{kg/m^3}$, $\mu_l = 8.91 \times 10^{-4}\,\mathrm{Pas}$, $\mu_g = 1.85 \times 10^{-5}\,\mathrm{Pas}$, $c_l = 4.18 \times 10^3\,\mathrm{J/kgK}$, $c_g = 1.01 \times 10^3\,\mathrm{J/kgK}$, $\lambda_l = 0.595\,\mathrm{W/mK}$, $\lambda_g = 2.55 \times 10^{-2}\,\mathrm{W/mK}$, $D_g = 2.6 \times 10^{-5}\,\mathrm{m^2/s}$, $\sigma_{\mathrm{ref}} = 7.2 \times 10^{-2}\,\mathrm{N/m}$, and $|\sigma_T| = 1.48 \times 10^{-4}\,\mathrm{N/mK}$. The dilute diffusion coefficient of particles is chosen as $D_{po} = 5 \times 10^{-12}\mathrm{m^2/s}$ based on $d_p = 0.1\,\mu\mathrm{m}$. The saturated vapor pressure is evaluated as a function of temperature

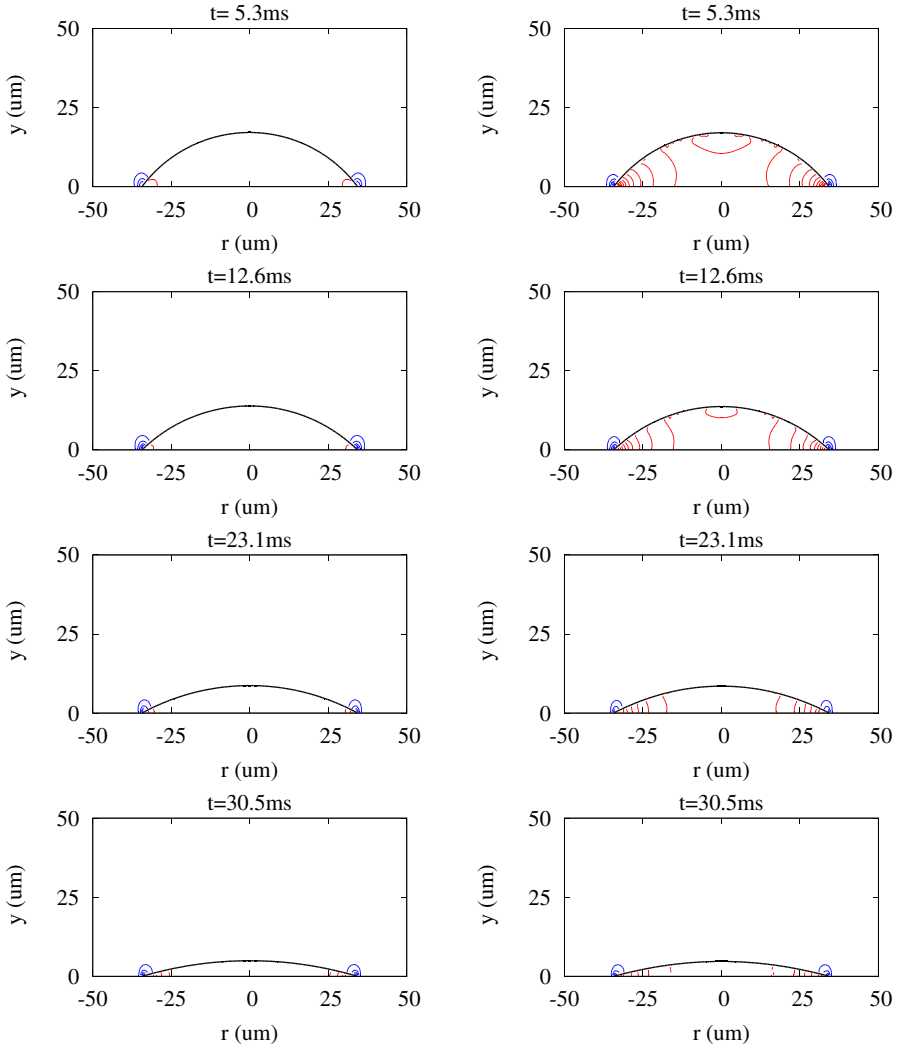


**Fig. 3.** Pressure fields in microdroplet evaporation (a) without and (b) with the Marangoni effect. The intervals between pressure contours are $1\,Pa$ in the gas region and $30\,Pa$ in the liquid region, respectively.

from the steam table [26]

$$p_{v,sat}(T_I) = \exp\left(9.487 - \frac{3.893 \times 10^3}{T_I + 230.47}\right) \tag{37}$$

where $p_{v,sat}$ is given in MPa and $T_I$ in °C.

Considering the experimental conditions of Lim et al. [27] for the evaporation of a pure water droplet, we choose the initial droplet radius as $R_i = 21\,\mu$m, the initial temperature as $T_i = 25\,°$C, the wall temperature as $T_w = 70\,°$C, the advancing contact angles as $\theta_a = 58°$, and the vapor mass fraction at the boundary as $Y_{v,\infty} = 8.8 \times 10^{-3}$ based on the relative humidity of 45%. A large computational

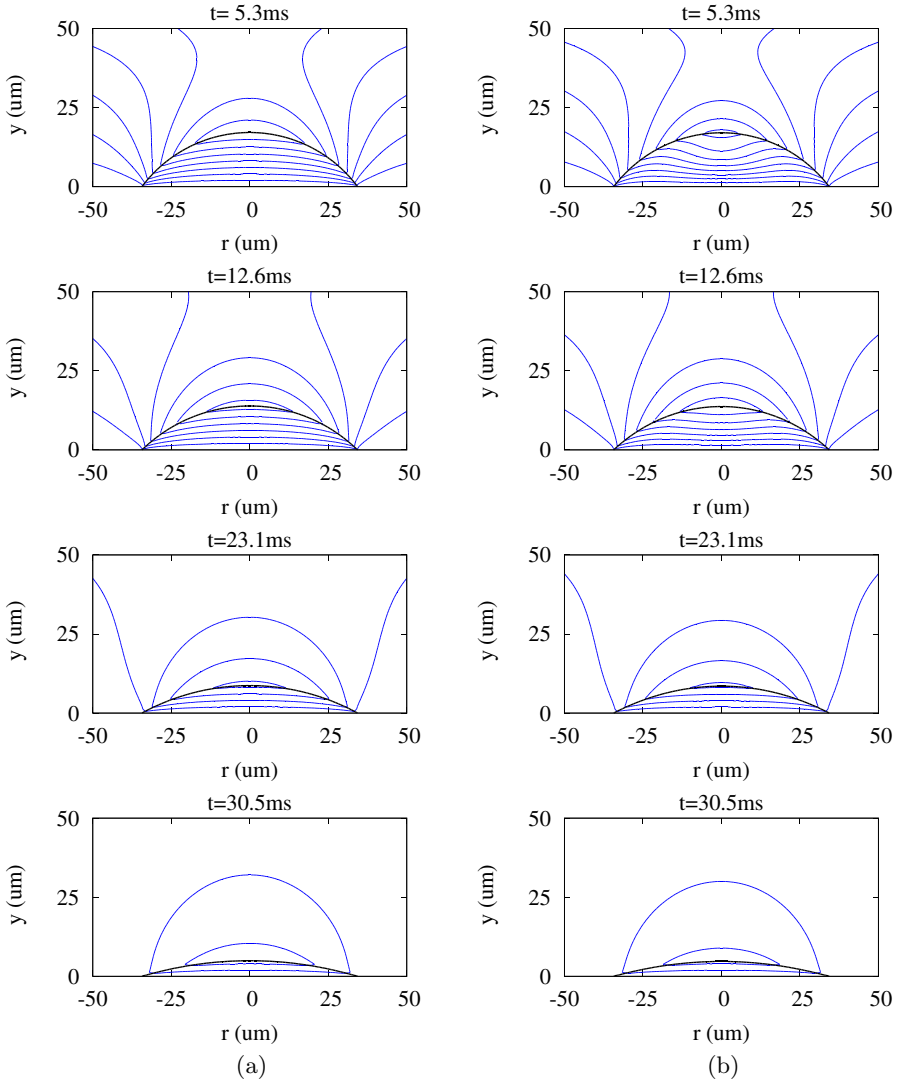


**Fig. 4.** Temperature fields in microdroplet evaporation (a) without and (b) with the Marangoni effect. The interval between temperature contours is 1 °C.

domain of $L = H = 773\,\mu$m is taken so that the droplet evaporation is not affected by the domain size. Uniform meshes with $h$ are used near the droplet, $r \leq 42\,\mu$m and $y \leq 42\,\mu$m, whereas nonuniform meshes with the ratio of two adjacent intervals of 1.1 are used for the other regions to save computing time. Initially, the droplet shape is taken to be a spherical cap with $\theta = 58°$ and the initial particle volume fraction as $Y_{p,i} = 0.05$.

A convergence test for grid resolutions is made with $h = 1.68\,\mu$m, $h = 0.84\,\mu$m and $h = 0.42\,\mu$m. The results are plotted in Fig. 1. The relative differences between the droplet-wall contact diameters and droplet volumes obtained from the successive mesh sizes are observed to be small as the mesh size decreases. The results obtained with $h = 0.84\,\mu$m almost overlap with $h = 0.42\,\mu$m. Therefore, most of computations in this study are done with $h = 0.84\,\mu$m to save the computing time, without losing the accuracy of numerical results.

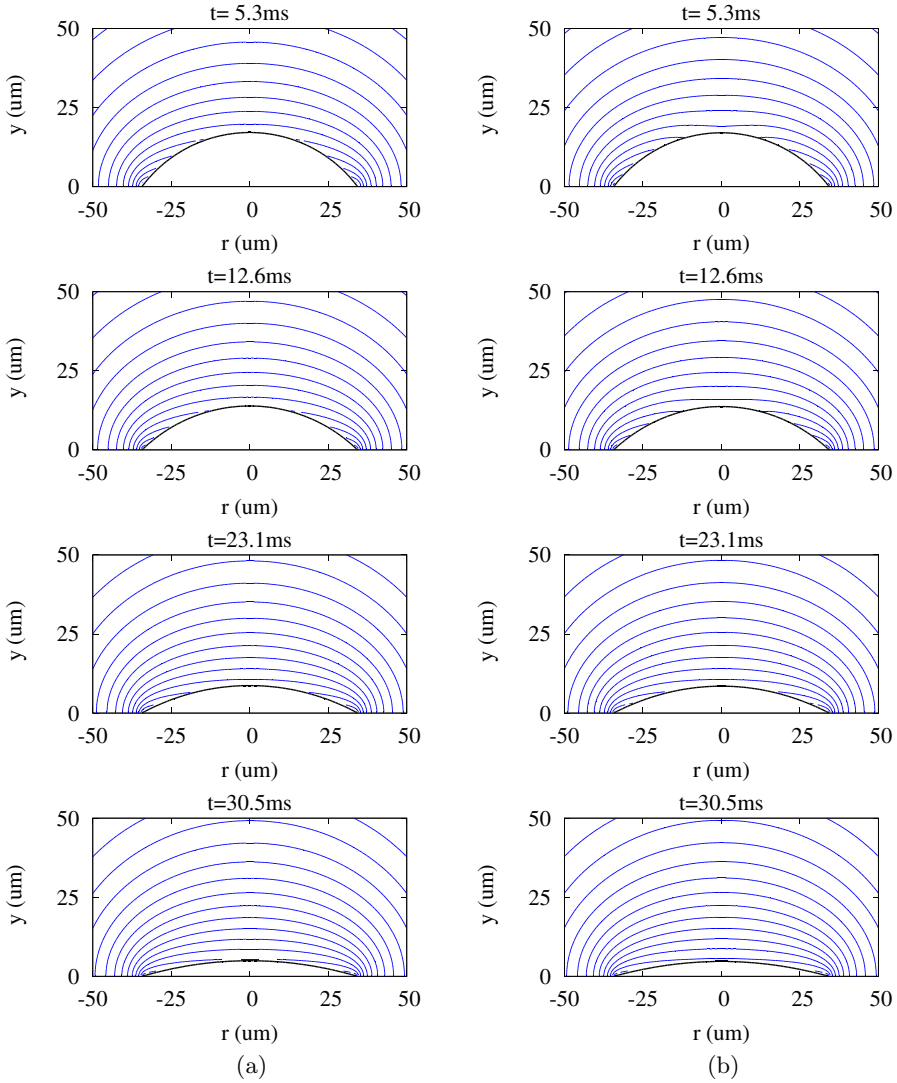


**Fig. 5.** Vapor fraction fields in microdroplet evaporation (a) without and (b) with the Marangoni effect. The interval between vapor fraction contours is 0.01.

Figure 2 shows the droplet motions and the associated velocity fields computed without/with the Marangoni effect. As the droplet volume decreases with evaporation, the contact angle decreases while the liquid-gas-solid contact line is fixed or pinned. In the case without the Marangoni effect, the liquid velocity is invisibly small in comparison to the gas velocity which is generated due to the liquid-vapor phase-change on the droplet surface and decays away from the liquid-gas interface. However, the case with the Marangoni or thermocapillary effect results in a significant increase of liquid velocity, as seen in Fig. 2b. The surface tension gradient due to the temperature variation on the droplet surface induces liquid and gas flows along the interface. The thermocapillary-driven liquid flows develop into clockwise and counter-clockwise circulations, as observed in the entire droplet region. The Marangoni flows decay as the interface temperature variation decreases with the heat transfer between the droplet and the solid surface. This velocity behavior affects the pressure field as seen

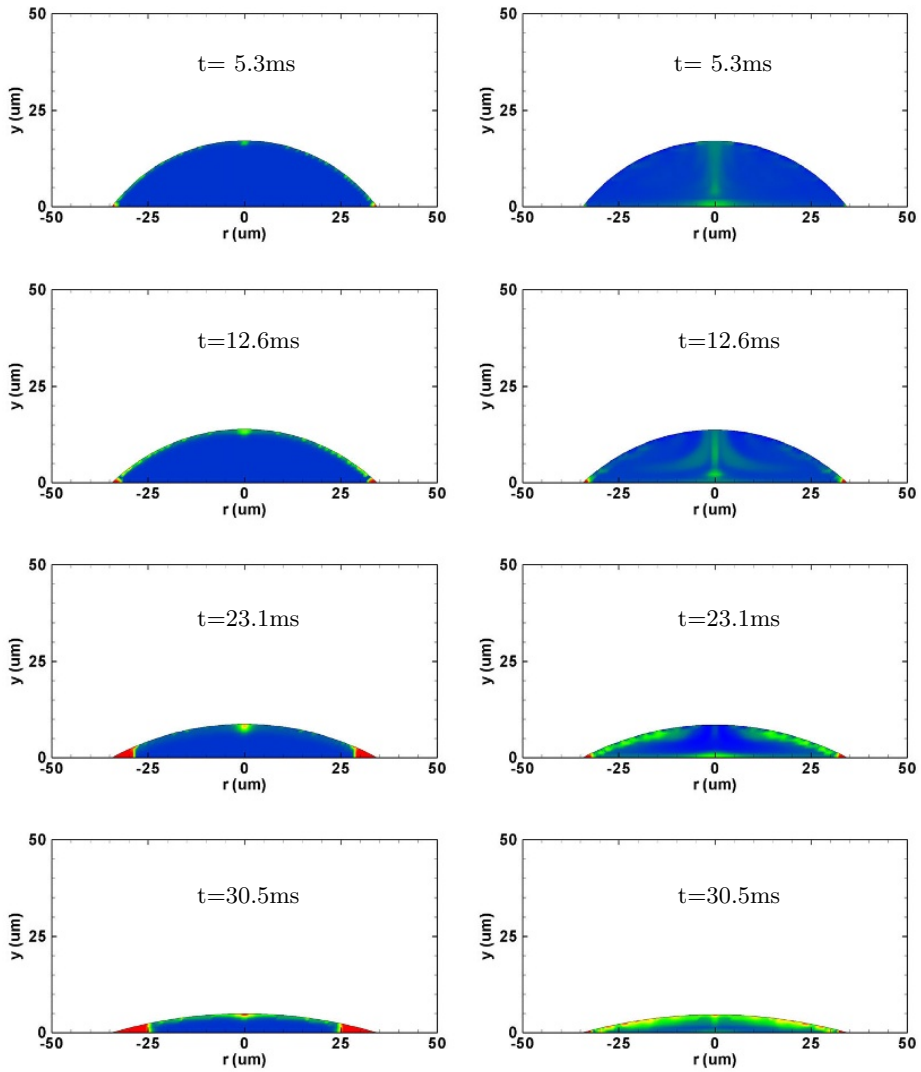


**Fig. 6.** Particle concentration fields in microdroplet evaporation (a) without and (b) with the Marangoni effect.

in Fig. 3. The pressure gradient is pronounced in the gas region near the liquid-gas-solid contact line and in the liquid region with the thermocapillary-driven flow.

The Marangoni effect on the temperature and vapor fraction fields are plotted in Figs. 4 and 5. Compared to the case without the Marangoni effect where the isotherms are parallel to the horizontal wall inside the droplet with negligible internal flow, the temperature fields in Fig. 4b with the Marangoni effect are disturbed inside the droplet and near the interface, but the thermocapillary effect is limited to the early period of droplet evaporation. It is noted that the temperature is not uniform along the interface, which results in the non-uniform vapor fraction distribution on the interface, as depicted in Fig. 5. The vapor fraction contours are more crowded near the lower portion of the interface with a higher temperature than the upper portion of the interface. This means that the evaporation rate is higher near the lower portion

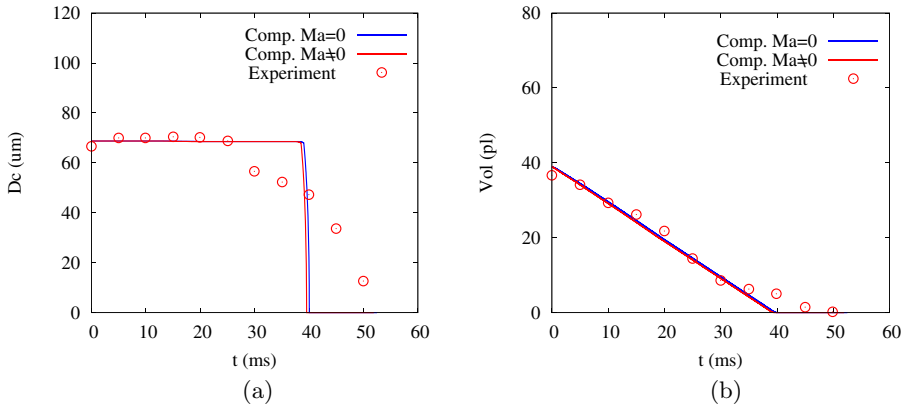


**Fig. 7.** Marangoni effect on microdroplet evaporation: (a) droplet-wall contact diameter and (b) droplet volume.

of the interface or the liquid-gas-solid contact line. The vapor fraction distribution is found to be little influenced by the Marangoni flow during the whole period of droplet evaporation.

Figure 6 shows the particle concentration fields. In the case without the Marangoni effect, as the non-uniform evaporation along the interface causes the liquid inside the droplet to move toward the contact line, the particles are accumulated near the contact line, as seen in Fig. 6a. However, the case with the Marangoni flow which is circulated along the interface toward the upper portion of the interface presents a significant change in particle distribution. When the thermocapillary-driven flow is pronounced during the early period of droplet evaporation, as depicted at $t \leq 12.6$ ms of Fig. 2b, the particle accumulation occurs near the center of solid surface due to the downward flow developed in the middle of the droplet. As time elapses and the Marangoni flow decays, the particle accumulation occurs in a wider region inside the droplet than the case without the Marangoni effect, as seen at $t = 30.5$ ms of Figs. 6a and 6b. This particle accumulation pattern in droplet evaporation dependent on the Marangoni effect is consistent with the observation of Hu and Larson [28].

The Marangoni effect on the temporal variations of the droplet-wall contact diameter and droplet volume is plotted in Fig. 7. The numerical results demonstrate the the Marangoni effect, which is an important parameter to determine the particle accumulation pattern, is negligible on the temporal variation of droplet shape and the evaporation rate. Compared with the experimental data of Lim et al. [27] for the evaporation of a pure water droplet with $\theta_a = 58°$ and $\theta_r = 25°$, the numerical prediction of droplet behavior shows a good agreement while the contact line is fixed, but it is deviated as the contact line of a pure droplet recedes. A particle-laden droplet, whose contact line is fixed during the whole period, is found to have a higher evaporation rate than a pure droplet. The evaporation period is shorter in the particle-laden droplet.

## 4 Conclusions

A level-set method, which is easily applicable to the liquid-gas interface with change in topology, was developed for comprehensive analysis of the evaporation of a particle-laden microdroplet on a solid surface including the effects of Marangoni or thermocapillary force and particle concentration as well as the effects of heat and mass transfer, evaporation, and dynamic contact angles. The computation without

the Marangoni effect shows that the droplet internal flow is invisibly small in comparison to the gas flow, and the particles are accumulated near the liquid-gas-solid contact line as the non-uniform evaporation along the interface causes the liquid inside the droplet to move toward the contact line. The case with the Marangoni effect results in a significant increases of the liquid velocity. When the thermocapillary-driven flow is pronounced during the early period of droplet evaporation, the particle accumulation occurs near the center of solid surface due to the downward flow developed in the middle of the droplet. During the late period of droplet evaporation, the Marangoni flow decays due to the heat transfer between the droplet and the solid surface, and the particle accumulation occurs in a wider region inside the droplet than the case without the Marangoni effect. However, the Marangoni effect is negligible on the temporal variation of droplet shape and the evaporation rate. A particle-laden droplet, whose contact line is fixed during the whole period, is found to have a higher evaporation rate and a shorter evaporation period than a pure droplet.

This work was supported by the National Research Foundation of Korea (NRF) funded by the Korean government (MSIP) (Grant No. 2013R1A2A2A01068333).

## References

1. R.D. Deegan, O. Bakajin, T.F. Dupont, G. Huber, S.R. Nagel, T.A. Witten, Nature **389**, 827 (1997)
2. B.J. Fischer, Langmuir **18**, 60 (2002)
3. E. Widjaja, M.T. Harris, AICHE J. **54**, 2250 (2008)
4. R. Bhardwaj, X. Fang, D. Attinger, New J. Phys. **11**, 075020 (2009)
5. K.L. Maki, S. Kumar, Langmuir **27**, 11347 (2011)
6. M. Fujita, O. Koike, Y. Yamaguchi, J. Comput. Phys. **281**, 421 (2015)
7. G. Son, J. Mech. Sci. Technol. **24**, 991 (2009)
8. G. Son, J. Heat Transfer **134**, 101502 (2012)
9. G. Son, Int. Commun. Heat Mass Transfer **58**, 156 (2014)
10. J. Lee, G. Son, Numer. Heat Transfer B **67**, 25 (2015)
11. V. Babin, R. Holyst, J. Phys. Chem. B **109**, 11367 (2005)
12. R. Holyst, M. Litniewski, D. Jakubczyk, M. Zientara, M. Wozniak, Soft Matter **9**, 7766 (2013)
13. R. Holyst, M. Litniewski, D. Jakubczyk, K. Kolwas, M. Kolwas, K. Kowalski, S. Migacz, S. Palesa, M. Zientara, Rep. Prog. Phys. **76**, 034601 (2013)
14. M. Kang, R.P. Fedkiw, X.-D. Liu, J. Sci. Comput. **15**, 323 (2000)
15. D.Q. Nguyen, R.P. Fedkiw, M. Kang, J. Comput. Phys. **172**, 71 (2001)
16. F. Gibou, R.P. Fedkiw, L.T Cheng, M. Kang, J. Comput. Phys. **176**, 205 (2002)
17. I.M. Krieger, Adv. Colloid Interface Sci. **3**, 111 (1972)
18. A.A. Potanin, J. Colloid Interface Sci. **157**, 399 (1993)
19. L. Daubersies, J.-B. Salmon, Phys. Rev. E **84**, 031406 (2011)
20. S.S.L. Peppin, J.A.W. Elliott, M.G. Worster, J. Fluid Mech. **554**, 147 (2006)
21. G.P. Sasmal, J.I. Hochstein, J. Fluids Eng. **116**, 577 (1994)
22. J.-J. Xu, W. Ren, J. Comput. Phys. **263**, 71 (2014)
23. M. Sussman, M. Ohta, SIAM J. Sci. Comput. **31**, 2447 (2009)
24. M. Sussman, Int. J. Numer. Meth. Fluids **68**, 1343 (2012)
25. J. Fukai, Y. Shiiba, T. Yamamoto, O Miyatake, O. Poulikakos, C.M. Megaridis, Z. Zhao, Phys. Fluids **7**, 236 (1995)
26. F.I. Jr. Thomas, E.L. Peter, *Steam and Gas Tables with Computer Equations* (Academic Press, 1984)
27. T. Lim, S. Han, J. Chung, J.T. Chung, S. Ko, C.P. Grigoropoulos, Int. J. Heat Mass Transfer **52**, 431 (2009)
28. H. Hu, R.G. Larson, Int. J. Phys. Chem. B **110**, 7090 (2006)